Peridynamic Approach to Digital Image Correlation Strain Calculation Algorithm

Tomas Vaitkunas [1,*]**, Paulius Griskevicius** [1] **and Adi Adumitroaie** [2]

[1] Department of Mechanical Engineering, Kaunas University of Technology, Studentu 56,
    LT-51424 Kaunas, Lithuania; paulius.griskevicius@ktu.lt
[2] Department of Intelligent Technologies, Institute of Fundamental Technological Research IPPT,
    Polish Academy of Sciences, Adolfa Pawinskiego 5B, 02-106 Warsaw, Poland;
    a.adumitroaie@structuralintegrity.eu
*   Correspondence: tomas.vaitkunas@ktu.lt

Abstract: Digital image correlation is an experimental optical non-contact full field displacement and strain evaluation method based on the surface subsets tracking with photo cameras, digital images processing, and numerical computation. However, the full field of strain computation is a challenging problem, mainly because the displacement field to be differentiated is not continuous, individual subsets are tracked by the optical digital image correlation system. Moreover, the numerical differentiation can also amplify the noise of the displacement field inducing thus strain errors when the displacement data are poor. The peridynamics theory (which equations are cast in terms of spatial integrals of displacements, instead of spatial derivatives in the classical continuum mechanics) based algorithm is considered in this study and applied for the experimental digital image correlation displacement field to analyze possible peridynamic differentiation method advantages. A strains convergence analysis between the digital image correlation and peridynamic differentiation methods is done in this study. The integro-differential strain calculation as an alternative method is validated against digital image correlation and finite element simulation strain fields. It is also shown that the digital image correlation, a noisy displacement field, still provides an accurate and low level noise strain evaluation based on the proposed method.

Keywords: strain field; digital image correlation; peridynamics; differentiation; peridynamic differential operator

1. Introduction

Developed in early 1980s, digital image correlation (DIC) system is an optical experimental method based on digital image processing and numerical computing [1–3] to measure full field displacement and strain on almost any solid material surface. The results of DIC are readily comparable with finite element (FE) results [4] or strain gauges [5]. Since the beginning of the DIC system development, its working principles and errors estimation has always been an interesting area of research. Pan et al. [1] and Sutton et al. [3] described the DIC system working principles and McCluskey [6], Bornert et al. [7], Siebert et al. [8] identified possible error sources which can cause displacement and strain measurement errors.

While the full field displacement can be directly calculated based on comparing subsets in images taken from deformed and undeformed object surface, the full field strain evaluation requires additional post-processing of the discrete displacement data points, namely numerical differentiation, which is based on interpolation functions of the discrete displacement field applied over subset areas of the entirely full field area, which subsets are defined according to an user-specified size and step periodicity. Numerical differentiation in mathematical theory is considered as an "unstable and risky operation" [9]. First

of all, differentiation-based methods face with deficiencies for problems involving discrete/discontinuous fields. Further, finite difference approaches are sensitive to noise. Pan et al. [10] demonstrated that if the measurement error of displacements is ±0.02 px and the DIC grid step is 5 pixels, then the error of strain calculation by forward difference is 8000 με. An error of this magnitude will hide the underlying strain information and the strain result will be worthless in most cases. The problem of strain measurement for a plate with circular hole under tension from the 2D DIC challenge 1.0 Sample 12 [11] was analyzed by several authors [12–14] (Figure 1). The exact strain solution for this problem is not given and can be only predicted by comparing with FE simulation or other numerical/experimental methods.
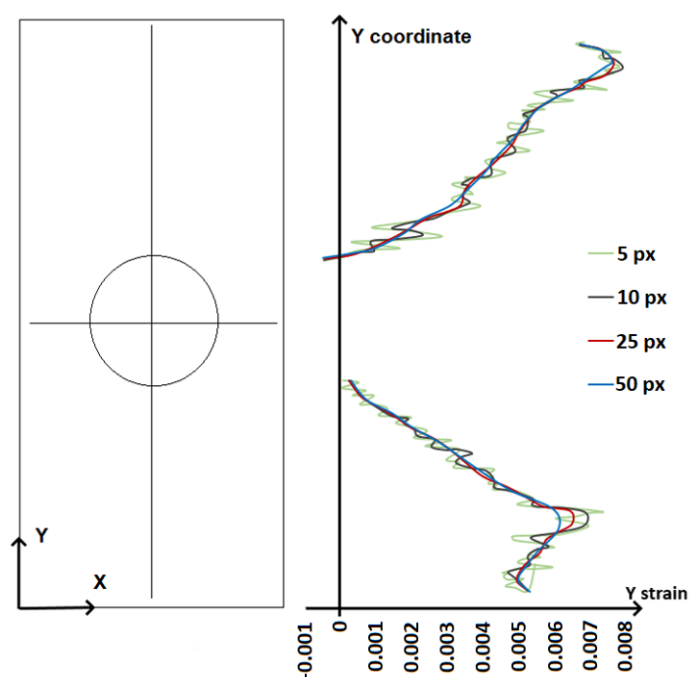

Figure 1. Plot (replicated from [12–14]) of the DIC evaluated strain for a plate with hole loaded in tension for various values of the DIC step.

It is visible from Figure 1 that increasing the DIC step size leads to a smoother strain profile but decreases accuracy due to the averaging effect of a larger DIC virtual strain gauge [12–14]. The strain results lead to the necessity to find the trade-off between accuracy and smoothness. Large strain gradients cannot be captured if too much smoothing is introduced, leading to poor accuracy. Conversely, resolving steep gradients leads to a highly oscillatory solution [15,16].

In order to overcome this issue, several improved differentiation techniques in DIC were offered. Zhao et al. [17] used modified Hermite finite element approach to ensure the smoothness and continuity of the strain field. A new nonlocal strain calculation method for DIC systems, based on a Kernel function built up from tensor products of functions that integrate to zero over domain, was proposed by Turner et al. [12]. The method is effective for problems with step gradients and when the displacement data is noisy. This specially applies to the fracture experiments [18,19] due to traditional DIC differentiation algorithms difficulties obtaining crack paths. In addition to this, other approaches were proposed to solve the differentiation issue in discontinuous DIC field. Chen et al. [20] developed a two-step X-DIC to minimize the errors in computing discontinuous full-field displacements. Fagerholt et al. [21], Yang and Bhattacharya [22] used mesh adaptations for measuring discontinuous fields in specimens with cracks. Similar technique based on both computed displacement and strain correlation was introduced by Yang et al. [23]. Methods relying on a subset split strategies measuring the

"displacement jumps" due to discontinuity and displacements and strains around the discontinuity were also developed [24,25].

The non-local peridynamics (PD) theory of continuum mechanics based on integral formulation of the equations of motion was developed by Silling in 2000 [26]. Due to not including local spatial derivatives into the formulation, the PD theory is very promising for applications to discontinuous fields [27,28]. Although the PD theory is defined in terms of the stretch between material points and the conventional continuum mechanics quantities of strain and stress are not PD theory conventional parameters, strains can still be retrieved in PD by the use of the PD integro-differentiation. The peridynamic differential operator (PDDO) was created for this purpose [29]. PDDO is always valid, even in the case of discontinuity. Madenci et al. [29–31] demonstrated other possible applications of the PDDO, for example, signal and images processing, data smoothing and noise reduction, data compression and recovery, interpolation and other mathematical operations.

Coupling between the two aforementioned methods, namely the experimental DIC and the computational PD, has also been of recent interest. Madenci et al. [32] used PD for tracking crack propagation paths. In their study displacements are imported from DIC measurements and used to calculate crack path using the PD simulation and PD damage parameters. Turner [33] and Li et al. [34] coupled DIC with PD simulation by reading the displacement field from DIC measurements and using it in PD simulations to circumvent the DIC difficulties when measuring full field deformations in discontinuous displacement field. The method was also applied to potential damage regions determined according to the low DIC correlation coefficients. According to their results, the authors claim that their coupled DIC and PD strategy can be used to predict both macro damage evolution and invisible micro-crack initiation and propagation before macro-crack forms.

Despite the work mentioned before related to DIC-PD coupling, the topic is still a very new one and of high potential to contribute to and enhance the capabilities of both experimental DIC and computational PD methods. Moreover, applying PDDO directly to DIC displacement field rather than coupling DIC displacement with PD simulations (this was done in studies [32–34]) brings new approach to be investigated. The aim of this study is to investigate into the possible applications of the PDDO to full field DIC in order to find possible improvements of the DIC differentiation algorithm and thus the DIC strain calculation accuracy. The problem of the plate with circular hole under tension is analyzed here, as means of introduction (Figure 1) the displacement and strain field gradients which pose a challenge for the conventional DIC calculation algorithm. The PDDO is used as a mathematical tool in order to differentiate the DIC discrete displacement field, for the cases of high gradients and oscillatory/noisy DIC data. Moreover, the proposed DIC-PDDO method performance against conventional DIC algorithms is evaluated based on the benchmark data from DIC Challenge 2.0 [11] and Metrological Efficiency Indicator (MEI) [35,36] which combines both spatial and measurement resolutions. Finally, the PDDO applications for faulty DIC data to recover the correct strain field are also analyzed.

The manuscript is organized as follows: brief review of the theoretical background related to the conventional DIC strain calculation and PD-PDDO theory is presented in Section 2; methods related to the experimental setup and computational models are presented in Section 3; results including a benchmark analysis of strains as calculated by conventional DIC, PDDO applied to DIC displacement data, and FE simulation are presented in Section 4. The results presented here can help to better understand the DIC method capabilities and the PDDO differentiation method potential to improve the DIC results.

2. Theoretical Background

2.1. DIC

The DIC working principle is based on optical tracking of displacements of subsets on the specimen surface during the specimen deformation. The general 3D DIC setup is shown in Figure 2a, (only basic DIC principles are presented in this chapter without going

into the details of 3D DIC and differences compared to 2D DIC, which can be found in elsewhere [3]).
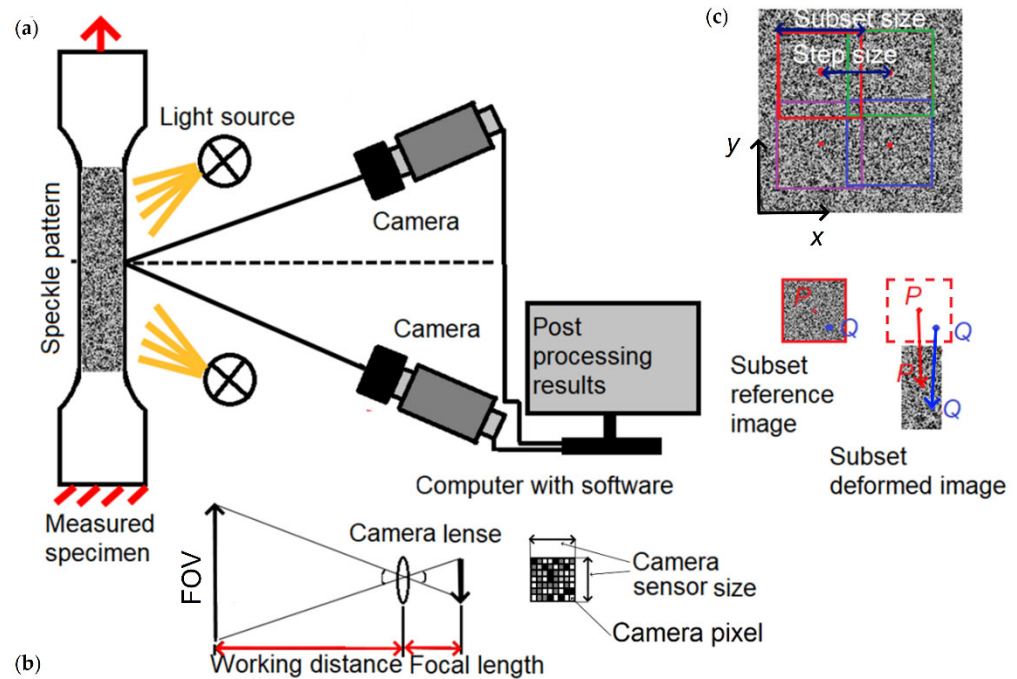

Figure 2. 3D DIC: (**a**) general experimental setup; (**b**) cameras and lenses parameters; (**c**) results post processing: subset tracking and displacement/strain calculation.

The DIC method consists of three steps: specimens preparation, recording images, and post processing computation. First, the pattern of points to be tracked is applied on the specimen surface during the preliminary stage of the specimen preparation, generating the so-called speckle pattern (Figure 2a). Painting the speckle dots on the specimen surface by using, for example, an air brush or a speckle pattern painting roller, is a popular method due to its simplicity and high enough quality for the DIC procedure, although other methods can be applied for specific materials (e.g., computer generated patterns printed on stickers, powder particles, laser engraving, etc.) [37].

Then, displacements of the speckle pattern points subsets are tracked with the optical cameras and recorded during the specimen deformation. Camera selection is based on the proper magnification which depends on the measuring scale of the test specimen. The specimens measuring area (FOV), camera sensor size, and the focal length of the lenses used with the camera are necessary to determine the magnification and working distance of the camera and thus its applicability for particular objects measurements [38]. Some of these parameters are shown in Figure 2b. Perfect camera focus and specimen lighting are required and can be achieved by adjusting the camera and light source to have enough exposure of the specimen (while avoiding over exposure). Some noise caused by the camera sensor, electronics, and lighting fluctuations is unavoidable, but its effect on measurement results can be minimized by a properly selected DIC setup [39].

Finally, the sequence of images recorded during the specimen testing and the corresponding speckle pattern deformation is analyzed by the DIC software during the post processing calculation stage [1,3]. The calculation procedure starts with dividing the whole FOV speckle pattern into a grid of sub-areas called subsets (see Figure 2c). The center of each subset (point $P(x_0, y_0)$ in Figure 2c) is the point where the displacement assigned to each subset is calculated. After the deformation of the test specimen and speckle pattern, the subset from the deformed image is compared based on correlation criterion calculations against the subset from the reference image to find the displacement of each subset center point $P(x_0, y_0)$ (Figure

2c). In order to define the position of the internal subset points $Q(x_i, y_i)$ after the subset deformation, displacement mapping by using the so called "subset shape functions", based on deformation continuity principle is done. The subset shape function cannot be selected by the user in the VIC-3D software used in this study [40]. The possibility exists that a point $Q(x_i, y_i)$ in the deformed image is located between the pixels of DIC sensor, and because of this a sub-pixel interpolation is necessary to define the displacement vector of that point. Several sub-pixel displacement interpolants (4th, 6th, and 8th orders polynomials) are available as user choice in the VIC-3D software [40].

Although the displacements of the DIC grid points (the centers of the grid subsets $P(x_0, y_0)$ in the Figure 2c) are measured directly, strains require additional mathematical operations, namely numerical differentiation, which can be performed in several different ways in a DIC algorithm: "subset shape function" differentiation, displacement field division into triangle finite elements and then their numerical differentiation, derivatives of local analytical equations defined over the selected size of local regions and approximating the displacement field, displacement field spline fit differentiation [38]. The principle of differentiation algorithm of the DIC post processing software VIC-3D from Correlated Solutions [41] used in this study is shown in Figure 3a. A grid of triangles (similar to FE triangular mesh) having the subsets center points of known displacement data at their vertexes is used. The strain distribution over each triangle is calculated from the deformed shape of each triangle FE element based on the strain shape functions defined over each triangular finite element.

Because the edge length of each triangle is about several pixels, strain results without additional smoothing techniques would be noisy. Because of this, DIC strain filters which smoothen the strain results over the strain filter area (Figure 3b) are applied. The filter size is a user defined parameter which can be expressed by the number of the DIC step sizes (e.g., filter 5–5 steps sizes, filter 35–35 step sizes, etc.). The DIC user should select between the high noise when using a small size strain filter vs low accuracy when using large strain filter (Figure 3b).
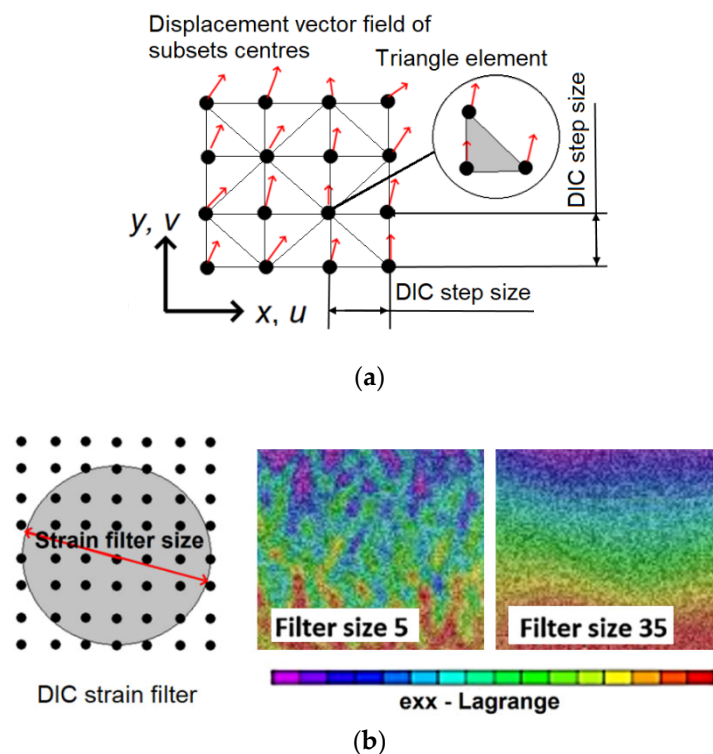

(**a**)

(**b**)

Figure 3. Strain calculation in the DIC software VIC-3D: (**a**) triangular mesh for strain calculation; (**b**) strain.

The subset size and the distance between two consecutive subset centers denoted as the step size are also user-defined parameters related to images post-processing, see Figure 2c. Although the proper subset size selection guidelines is given in the literature and DIC manuals [6,37], to make the subset size selection easier for the user, the DIC software calculates default subset values according to the speckle size. The general recommendation for the step size selection is about 1/4 of the value of subset size [42]. The step size is related to the spatial resolution (although the subset size and shape function have much higher effect on it) of the DIC measurements because with a smaller step size more DIC data points are taken and the resolution of the results increased, but the computation time and noise increase as well [42].

The proper DIC parameters selection for each step of the method (namely specimen preparation, images recording and images post processing) has an impact on the DIC results accuracy, especially strains. The main DIC parameters affecting the results accuracy are summarized in Table 1. This study deals with the DIC step size (ST) and strain filter size (FS) which together with the subset size (SS) can be combined to a single parameter, called virtual strain gauge (VSG) and expressed as [38]:

$$\text{VSG} = (\text{FS} - 1) \cdot \text{ST} + \text{SS}. \tag{1}$$

VSG influence on the DIC strain results accuracy and the possibility to improve the strain results accuracy by using the PDDO to differentiate DIC displacement field are analyzed in this study.

Table 1. DIC parameters determining the measurements accuracy.

Specimens Preparation	Experiment	Post Processing
Speckle size Speckle pattern quality (randomness, contrast, etc.)	Calibration Camera resolution Camera focus Lightning Camera noise	Subset size Step size Subset shape function Displacement sub-pixel interpolation Strain filter size

2.2. Peridynamics Theory and Peridynamics Differential Operator

The peridynamics (PD) theory [26,43] reformulates the classical continuum mechanics theory by including spatial integrals instead of spatial derivatives in its equations of motion. Owing to this feature, the PD model enables the possibility to effectively simulate discontinuities (e.g., cracks, defects) without the need of any additional models. In the PD model the domain is discretized into a square grid of equally spaced material points (PD grid spacing Δx, see Figure 4) and each material point x, defined by the position vector $\boldsymbol{x}$, interacts with the material points x' in the interaction range H_x called PD horizon, which is a measure of the material non-local behavior defining the range of interaction of the material points. The horizon size δ is, usually expressed as a radius equal to a multiple of the PD grid spacing $\delta = m\Delta x$ (Figure 4). According to studies on the parameter m [44], a PD horizon of about $3 \cdot \Delta x$ ensures the PD model stability and convergence in most cases. The PD model grid size Δx should be selected to evaluate the local effects with suitable accuracy, and can be found based on results of convergence analysis. The interaction between the PD points x and x' is called PD bond, and the deformation of the body (displacement vectors $\boldsymbol{u}$ and $\boldsymbol{u}'$ of points x and x') causes deformation of the PD bonds and thus forces $\boldsymbol{f}$ and $\boldsymbol{f}'$ acting on the PD bonds between the points x and x'.
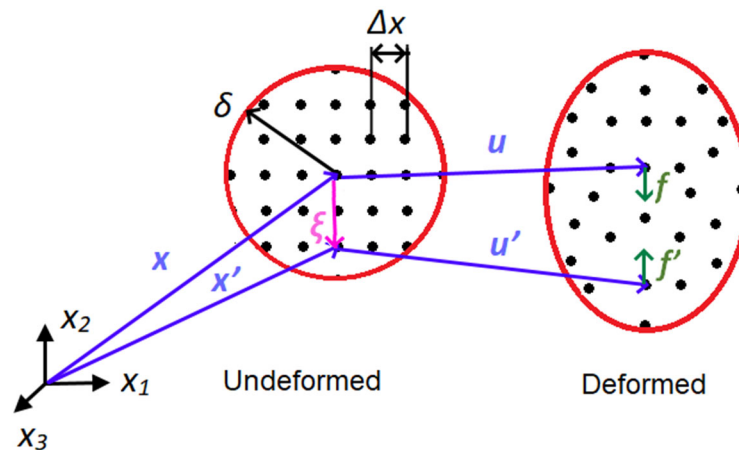
Figure 4. The basic principles of the PD theory.

Due to formulation of bond forces *f* and *f'* being opposite in direction and of equal magnitudes (bond-based PD), interactions of a material point to other points are limited in the range of the PD horizon and it results that the Poisson's ratio can only be 0.25 for 3D case and 0.33 for plane stress case [45]. This limitation is released by including new mathematical operators–deformation and forces states (state-based PD) in the PD theory resulting that the PD bond forces are not equal in magnitude (PD bond force depends on the current bond deformation and the deformation of all other bond connecting the same point). The PD states map undeformed horizon points on any deformed configuration of the horizon (detailed description of the PD states can be found in [45]). The state-based PD equation of motion is written as:

$$\rho \ddot{\boldsymbol{u}}(\boldsymbol{x},t) = \int_{H_x} \{\underline{\boldsymbol{T}}[\boldsymbol{x},t]\langle \boldsymbol{x}'-\boldsymbol{x}\rangle - \underline{\boldsymbol{T}}[\boldsymbol{x}',t]\langle \boldsymbol{x}-\boldsymbol{x}'\rangle\}dV_{x'} + \boldsymbol{b}(\boldsymbol{x},t), \qquad (2)$$

where ρ is the material density, $\boldsymbol{b}(\boldsymbol{x}, t)$—body forces, and Vx—volume of the point *x*. $\underline{\boldsymbol{T}}[\boldsymbol{x},t]\langle \boldsymbol{\xi}\rangle$ is a force state valued function of position *x* and time *t* and operating on the vector $\boldsymbol{\xi} = \boldsymbol{x}' - \boldsymbol{x}$ (Figure 4).

The classical continuum mechanics concepts of strains and stress are not included in the PD theory, their PD equivalents being the PD bond stretch and the PD bond force. However, retrieving the conventional strain quantities from the PD formulation is possible based on differentiation of the integral PD equations of deformation. Derivatives of the discrete (PD grid) PD field, even in the presence of discontinuities, can be found by applying the peridynamic differential operator (PDDO) [29,30].

According to the PD theory [26,43], the variation of a scalar field $f = f(\boldsymbol{x})$ at the point *x* is influenced by its interaction with other points *x'* in the horizon H_x (Figure 4). Moreover, the degree of interaction between the PD points is specified by a nondimensional weight function $\omega(|\boldsymbol{\xi}|)$ which reflects the degree of non-locality among the points of the domain. The weight function ω is chosen such that it captures the physical characteristics of the material behaviour, namely decreasing degree of interaction with increasing distance $|\boldsymbol{\xi}|$ between the points. The PDDO allows for the calculation of the spatial derivatives of the field function $f = f(\boldsymbol{x})$ based on integral equations. For the 3D case (Figure 4), the expression of the PDDO for the first order derivatives of the function *f* can be derived as [29,30]:

$$\frac{\delta f}{\delta x_i} = A^{-1} \int_{H_x} \omega(|\boldsymbol{\xi}|) f(\boldsymbol{x} + \boldsymbol{\xi})\xi_i dV, i = 1, 2, 3, \qquad (3)$$

where the quantity *A* is given by $A = \int_{H_x} \omega(|\boldsymbol{\xi}|) \begin{bmatrix} \xi_1^2 & \xi_1\xi_2 & \xi_1\xi_3 \\ \xi_1\xi_2 & \xi_2^2 & \xi_2\xi_3 \\ \xi_1\xi_3 & \xi_2\xi_3 & \xi_3^2 \end{bmatrix} dV$, and dV is the volume of the PD point. The effect of the weight function ω is analyzed in [38,39]. Selesona

et al. [39] concludes that a linear function (e.g., $\omega(|\boldsymbol{\xi}|) = \delta/|\boldsymbol{\xi}|$) is enough for 3D problems and a cubic order function is well suitable for 2D case.

In this way Equation (3) allows for an integral-based calculation of the derivatives of displacements u_1, u_2, u_3 at point x (by considering the function f in Equation (3) as u_1, u_2, u_3, respectively): ; $\nabla_o \boldsymbol{u} = \frac{\delta \mathbf{u}}{\delta \mathbf{x}}$; which allows for the calculation of the conventional continuum mechanics Lagrangian strain tensor at point x:

$$E = \frac{1}{2}(\nabla_o \boldsymbol{u} + (\nabla_o \boldsymbol{u})^T + \nabla_o \boldsymbol{u} \cdot (\nabla_o \boldsymbol{u})^T). \tag{4}$$

In the discretized form of Equation (3) (i.e., replacing the integral over the horizon H_x with summation over the PD points inside of the horizon), the function f in Equation (3) becomes the discrete values of the function at the discrete PD points inside of the horizon H_x.

3. Method

3.1. Experimental Setup

Synthetic DIC images from DIC Challenge [11] (DIC Challenge 2.0 Star 6 for PDDO performance evaluation, DIC Challenge 1.0 Sample 12–the same plate with hole as presented in Figure 1) and in-house experimental DIC measurements are considered for the PDDO applications to compute strains. Plate with hole tensile test specimens of dimensions 180 mm × 35 mm and hole diameter 10 mm were prepared for experimental DIC measurements. The plate material–DIBOND composite [46] is a sandwich material of total thickness 3 mm, composed of three layers: polyethylene core of thickness 2.4 mm, and aluminum EN AW 5005 external layers of thickness 0.3 mm. The PDDO code was used for strain calculation from the DIC displacement field, and because of this the material properties (Young modulus, Poisson ratio) are not required. No special testing standard was used for the specimen preparation because our purpose was to measure the strains near the hole with DIC rather than testing the material properties.

The (experimental) strain computation setup is shown in Figure 5. Strain computation stage using PDDO (only this stage was necessary for the strain computation from DIC displacements calculated from DIC Challenge [11] images) is excluded with dashed line in Figure 5. In order to perform a tensile test for experimental DIC measurements, an electromechanical testing machine INSTRON E10000 with maximum force 10 kN was used, and the specimen with hole was loaded in tension at 3 mm/min crosshead speed. The full field displacement and strain measurements were done with the 3D DIC system from Correlated Solutions [2] equipped with two CMOS cameras Basler acA4112 of 12 Mpx resolution, sensor size 14.1 mm × 10.3 mm, pixel size 3.45 μm × 3.45 μm, and lenses of focal length 25 mm. Adjustable power LED lamp ProfiluxLED1000 with maximum power 185 W was used as light source. A black dots speckle pattern of 0.18 mm size was painted on the specimen surface, previously coated with white paint, using a painting roller from Correlated Solutions. A total of 25 calibration images of a 14 × 10 dots calibration plate with 10 mm dots spacing were taken before the experiment to calibrate the DIC system.

The DIC displacements calculated from experimental and synthetic images were analyzed and based on them the DIC strains were computed by using the DIC software VIC-2D and VIC-3D [40]. The subset size was set to 29 px for experimental DIC measurements and 41 px for synthetic DIC images according to the system-suggested value and then step sizes were set equal to 1/4 of the subset sizes. The other parameters of DIC for all computations were set as default: normalized squared differences correlation criterion between undeformed and deformed speckle, and 6th order polynomial for the sub-pixel displacement interpolation. The *Exhaustive search* option was enabled resulting that all initially failed correlation between the tracked points is repeated [40] and more data points can be retrieved.
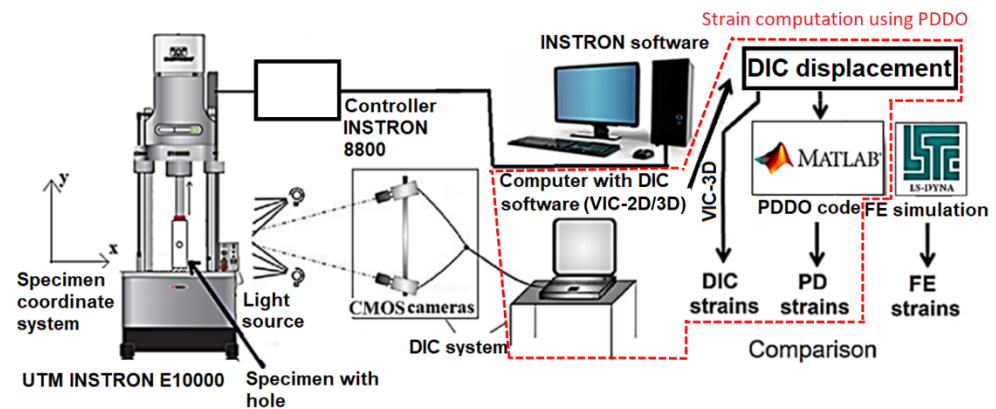
Figure 5. Schematic of the experimental-computational setup.

A number of 104 images of the DIBOND composite specimen were taken with the DIC system during the in-house experimental testing. The DIC displacements were exported from the VIC-2D or VIC-3D software to calculate strains by applying the PDDO (the DIC-PDDO strains). Moreover, in case of experimental DIC measurements, FE simulation of the specimen was performed in LS-Dyna to confirm the correctness of both in-house experimental DIC and DIC-PDDO strain fields.

3.2. PDDO Implementation

The PDDO (see Section 2.2) was applied to a regular square grid of PD points of both DIC Challenge [11] and in-house experiment virtual specimens surfaces, where displacements were measured from the images by DIC. For this purpose, the export data options *Pixel Grid* and *Metric nodes* in the DIC software VIC-2D and VIC-3D were used. These options enable to export points coordinates, their displacement and strain values from the DIC field over a selected regular square grid to .csv file. Then the exported DIC data from .csv file was directly imported to the PDDO code by ensuring the same location of the virtual and experimental specimens data points. When exporting the DIC displacement data at selected grid spacing to PDDO applications, the corresponding DIC step size adjustments are unnecessary. This is because only displacements are required for PDDO strain calculations and DIC VSG size has no effect on PDDO-calculated strains. Moreover, no additional data transformations (e.g., interpolation between the points, coordinates reposition) were applied in the PDDO code.

In order to find the value of the PD grid spacing Δx (see Section 2.2) for which the DIC-PDDO strains converge to the DIC strains, in-house experimental DIC displacement measurements data (DIBOND composite specimen data) were exported at different grid spacing values from VIC-3D to PDDO applications. The lower bound of the PD grid spacing can be considered equal to one DIC camera pixel size (on the specimen surface), which can be calculated as:

$$\frac{\text{FOV}}{\text{Camera sensor size}} \cdot \text{Camera pixel size} = \frac{180 \times 131}{14.1 \times 10.3} \cdot$$

(5)

$$3.45 \cdot 10^{-3} \times 3.45 \cdot 10^{-3} = 0.044 \text{ mm} \times 0.044 \text{ mm}.$$

To collect strain data only around the hole (high strain gradients can be captured in this region), a 30 mm × 30 mm square area of the DIBOND composite specimen surface around the hole was used for the DIC-PDDO calculation (see Figure 6a).
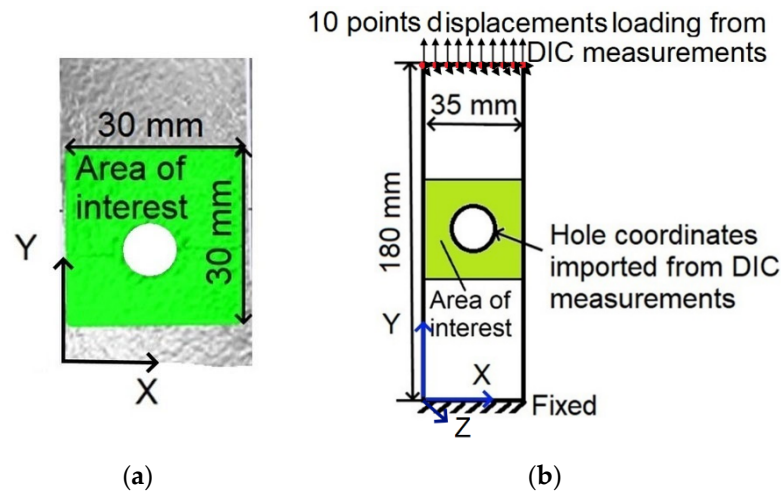
Figure 6. Computation scheme: (**a**) selected area of interest on the specimen surface for the DIC-PPDO calculation; (**b**) loading scheme of the specimen FE model.

The PDDO based on Equation (3) adopted for the 2D plane stress case was implemented in MATLAB. Basic MATLAB code principles were followed according to [47]. In order to find the 2D strain (displacement gradient $F(x_j)$) at point x_j from the discrete displacement data points, the integral Equation (3) is modified and discretized as summation of the n discrete data points over the integration domain:

$$F(x_j)_i = \left[\sum_{k=1}^{n} \omega(|\boldsymbol{\xi}_k|) f(\boldsymbol{x}_k + \boldsymbol{\xi}_k) \xi_i h \Delta x^2\right] A^{-1}, i = 1, 2, \tag{6}$$

where $\boldsymbol{\xi}_k = \boldsymbol{x}_k - \boldsymbol{x}_j$, $h\Delta x^2$ – 2D PD point volume. Substitution of the discretized form of $A = \sum_{k=1}^{n} \omega(|\boldsymbol{\xi}_k|) \begin{bmatrix} \xi_1^2 & \xi_1\xi_2 \\ \xi_1\xi_2 & \xi_2^2 \end{bmatrix} h\Delta x^2$ to Equations (2) and (3) finally results:

$$\boldsymbol{F}(x_j) = \left[\sum_{k=1}^{n} \omega(|\boldsymbol{\xi}_k|) \left((\boldsymbol{u}_k + \boldsymbol{x}_k) - (\boldsymbol{u}_j + \boldsymbol{x}_j)\right) \otimes \boldsymbol{\xi}_k\right] \cdot \left[\sum_{k=1}^{n} \omega(|\boldsymbol{\xi}_k|)(\boldsymbol{\xi}_k \otimes \boldsymbol{\xi}_k)\right]^{-1}, \tag{7}$$

here $\boldsymbol{u}_j$, $\boldsymbol{u}_k$ and $\boldsymbol{x}_j$, $\boldsymbol{x}_k$ are displacement and position vectors associated with the discrete points x_j, x_k (also see Figure 4). The MATLAB code calculates and plots the strain field using the DIC displacement field given at the regular grid of points on the specimen surface. The main parameters of the PDDO code are the horizon size δ and the weight function $\omega(|\boldsymbol{\xi}_j|)$ which in our case is defined as a $\omega(|\boldsymbol{\xi}_j|) = \delta^3/|\boldsymbol{\xi}|^3$.

3.3. FE Model

The FE model of the in-house test specimen was created in LS-PrePost 4.6 and simulation was run in LS-Dyna R11.0. The hole geometry was defined according to the specimen coordinates imported from DIC such that the hole shape in FE is not idealized but identical to the real shape and thus the strain concentration can be more effectively evaluated. The loading scheme of the model is shown in Figure 6b. The bottom of the FE model is fixed while the top is loaded by applied displacements in *X*, *Y*, *Z* directions which values were taken from 10 points DIC displacement measurements at the top of the specimen to reduce the errors due to possible specimen imperfect alignment in the testing machine.

Mixed quadratic-triangle fully integrated 1st order SHELL elements with an average element size of $5 \cdot 10^{-4}$ mm over the area of interest were used. The LS-Dyna material model PIECEWISE_LINEAR_PLASTICITY was selected. The material properties were measured according to inhouse tensile testing of the DIBOND composite plate without hole: the effective elastic modulus $E_f = 43$ GPa, effective Poisson ratio $\upsilon = 0.3$, and yield limit $\sigma_y = 100$ MPa. Moreover, the experimental tensile diagram was uploaded to the FE material model

by using the LS-Dyna material model curve definition keywords. Non-linear implicit time integration with Broyden–Fletcher–Goldfarb–Shanno algorithm [48] was used in LS-Dyna.

4. Results and Discussion

4.1. Effect of the PD Grid Spacing and PD Horizon Size

Plots of the absolute maximum values of the ε_x and ε_y Lagrangian strains computed on in-house tensile experiment specimen surface by applying the DIC-PDDO method, as function of the PD grid spacing Δx when the PD horizon size is fixed to $\delta = 3.1\Delta x$, are presented in Figure 7. Each dot in Figure 7 represents the DIC-PPDO maximum absolute strain value at selected PD grid spacing Δx, while the strain-PD grid spacing relation approximation with linear function is shown with dashed line. The same strain values calculated by the DIC algorithm for different setup values of the DIC VSG, are also plotted in Figure 7. The PD grid spacing Δx, as parameter independent on the particular specimen dimensions, is expressed as number of specimen pixels (calculated according to the Equation (5)).
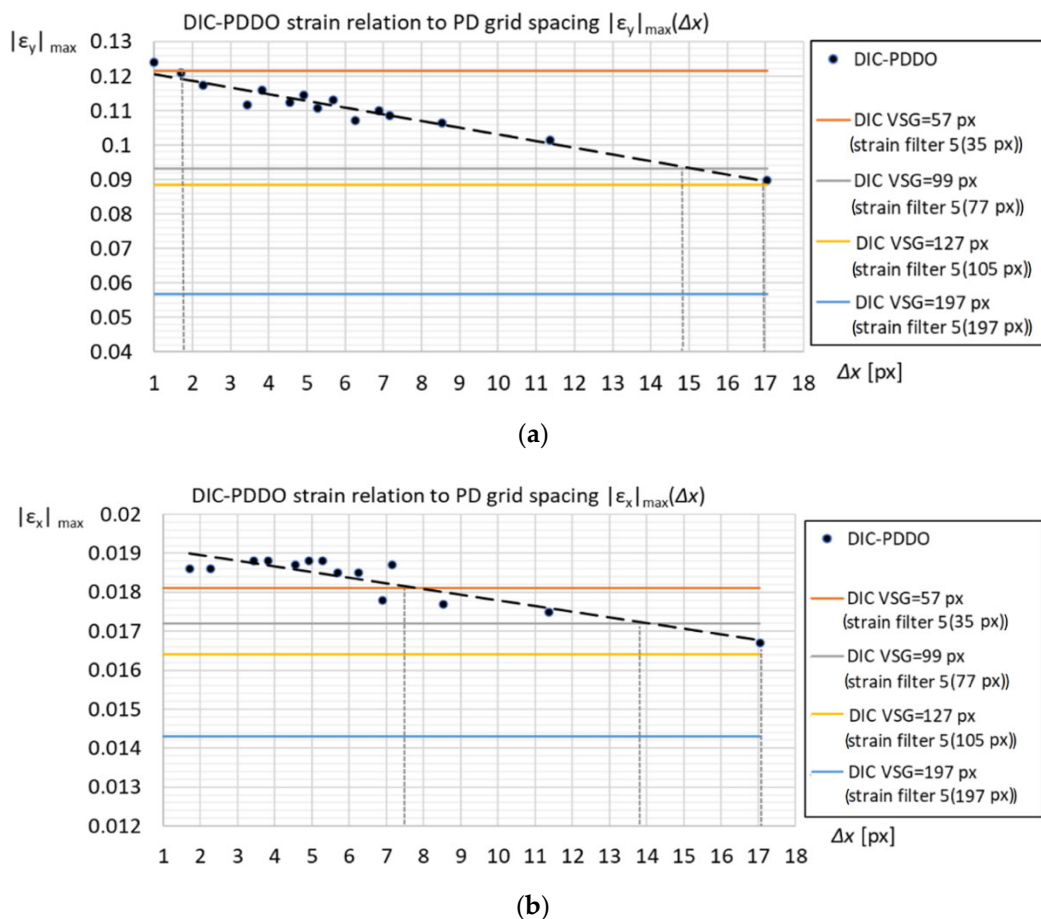

(**a**)

(**b**)

Figure 7. Effect of the PD grid spacing Δx on the strain values computed on in-house tensile experiment specimen surface by the DIC-PDDO method ($\delta = 3.1\Delta x$): (**a**) ε_y strains, (**b**) ε_x strains.

The results in Figure 7 show that the maximum values of $\left|\varepsilon_y\right|_{max}$, $\left|\varepsilon_x\right|_{max}$ absolute maximum strains are achieved for the minimum setup values for the PD grid spacing (for the DIC-PDDO strain calculation) and DIC VSG size (for the DIC strain calculation). This is because more localized strain values are calculated by decreasing the PD grid spacing

and the DIC VSG, avoiding thus the averaging effect when using larger PD grid spacing and DIC VSG.

Moreover, the results from the DIC-PDDO and DIC converge when using the minimum setup values for the PD grid spacing and DIC VSG showing thus the potential of the PDDO to capture localized strain values (situation in which the DIC results are highly prone to noise/oscillations [12–14], also see Figure 1). Relative differences of 1.6% for the ε_y and 2.6% for the ε_x strain components are obtained between the PDDO and DIC calculations, for the minimum setup value of 1 px for the PD grid spacing and VSG = 57 px for the DIC VSG.

The effect of the PD horizon diameter 2δ (measured in pixels) on the PDDO-calculated strain values, and comparison against the values calculated for different VSG sizes is shown in Figure 8 for the PD grid spacing $\Delta x = 1$ px. The same way as in Figure 7, the dots in Figure 8 represent the DIC-PPDO maximum absolute strain value at different PD horizon diameters while the linear strain-PD horizon diameter relationship is shown with dashed line. Although the same PD horizon size $\delta = m\Delta x$ can be achieved by taking different PD grid spacings Δx and multipliers m, our study shows that the maximum absolute strain value correlated well to the PD horizon size independently of the PD grid spacing Δx selected to achieve a particular value of the PD horizon in Figure 8.
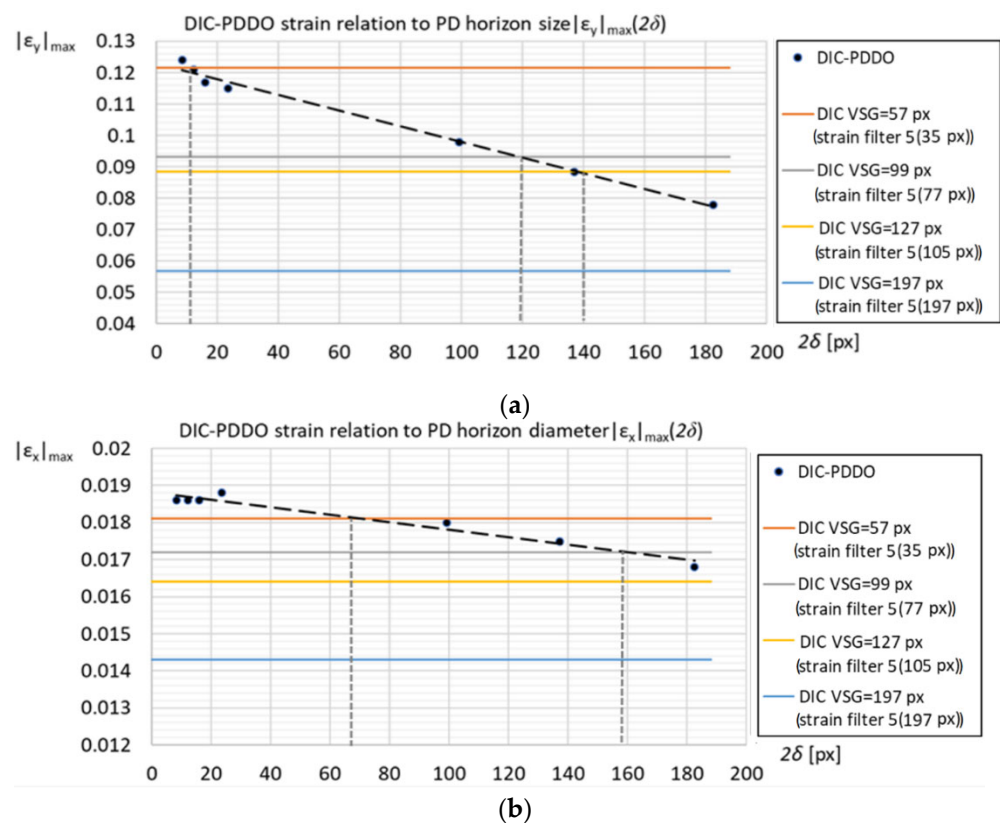

(a)

(b)

Figure 8. Effect of the PD horizon size on the strain values computed on in-house tensile experiment specimen surface by the DIC-PDDO method: (**a**) ε_y strains, (**b**) ε_x strains.

Similarly to the conclusions of Figure 7, the results in Figure 8 show that the maximum values of the PDDO strains are obtained for the minimum values of the PD horizon size and DIC VSG size, based on reduced strain averaging effect. The effect of the PD horizon for the PDDO method can be compared to the VSG/strain filter for the DIC method, namely strains peaks smoothening and averaging over the size of the horizon/filter, and the convergence of the PDDO and DIC strains with reducing the PD horizon size and the DIC VSG size can be noticed in Figure 8, which suggests the same possibility of using the PDDO strain calculation method to capture localized strains, for the situation

when strain oscillations are obtained based on reducing the DIC VSG (in this case strain filter) size.

4.2. DIC, DIC-PDDO and FE Strains Comparison

In order to validate the DIC and DIC-PDDO results, comparison of the DIC and DIC-PDDO strains against the FE simulation strains computed on in-house tensile experiment specimen surface is presented in Figure 9, showing a good agreement in terms of magnitude and location of maximum strains, as well as distribution and magnitude of the overall strain fields. Based on the results from Figures 7 and 8, VSG of size 57 px was used for DIC and the PD absolute horizon diameter of $2\delta = 24$ px (1.04 mm) was selected for DIC-PDDO. A difference of 8% for both $\left|\varepsilon_y\right|_{max}$ and $\left|\varepsilon_x\right|_{max}$ strains is obtained between the DIC-PDDO and the FE results. It is also worth noticing the asymmetric profile of the strain field in Figure 9 (which is due to imperfect circular profile of the central hole and imperfect alignment between specimen and loading in the testing machine; the method, used to evaluate and reduce those effects, is defined in Section 3.3) shows bigger differences between DIC and FE strains than the differences between DIC and DIC-PDDO strains. Moreover, DIC smears the maximum strain value near the hole and thus FE simulation results higher maximum strains. Nevertheless, strain fields, captured by the experimental DIC measurement can be validated by the FEA computational results and are well reproduced by the DIC-PDDO method in terms of both distribution and magnitude.
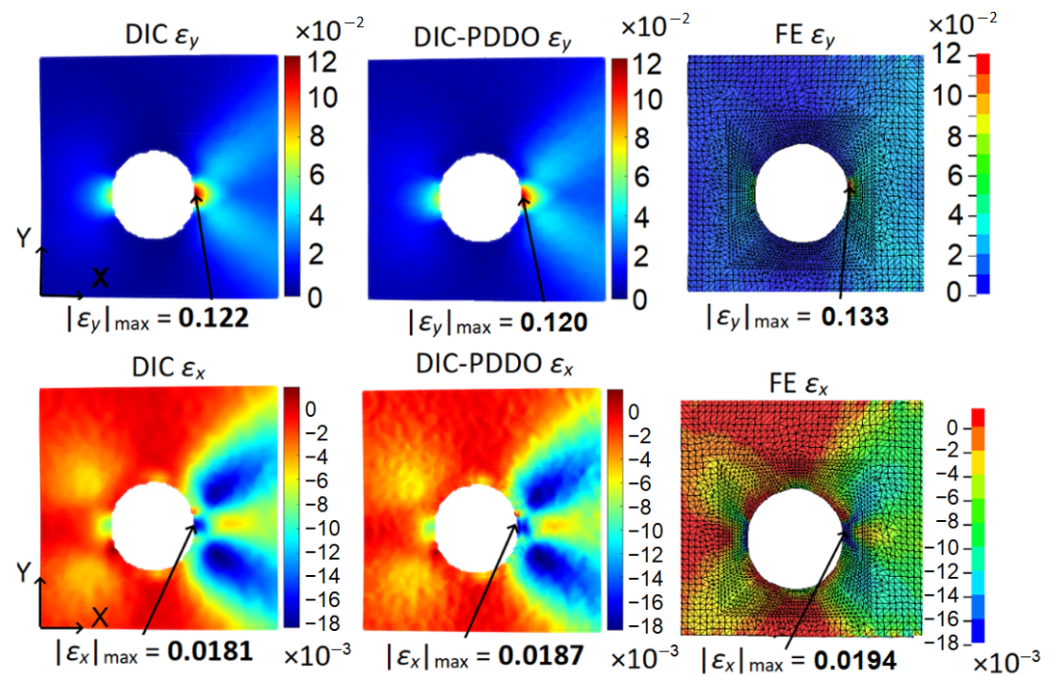

Figure 9. Comparison of ε_y, ε_x Lagrangian strains computed on tensile experiment specimen with DIC (VSG = 57 px), DIC-PDDO ($\delta = 3.1\Delta x, \Delta x = 0.167$ mm) and FE simulation.

4.3. DIC-PDDO Method Performance Evaluation

Despite the good agreement between DIC and DIC-PDDO strain fields noticed in Figure 9, a better metric should be used to evaluate the proposed DIC-PDDO strain computation method. Moreover, the agreement of maximum strain values is related to the spatial resolution not including the effect of measurement resolution. Recently created metrological efficiency indicator (MEI) [35,36] combines both spatial and measurements resolutions and for the case of strains is expressed as:

$$\text{MEI} = n^2 l_{10\%}, \tag{8}$$

where n is the standard deviation of the noise level in analyzed strains, $l_{10\%}$–cutoff period to the 10% fractional strain bias. Lower MEI values indicate better method performance.

The DIC Challenge 2.0 [11] Star 6 synthetic images are used to evaluate the DIC-PDDO method against conventional DIC. Star 6 contains 3 speckle images: an unde-formed reference; one deformed image (sinusoidal vertical strain amplitude of 5% "star" pattern is used to calculate the strain spatial resolution); and a noise floor image to calcu-late the measurement resolution. According to the MEI calculation procedure and Star 6 images definition found in [35], the cutoff period $l_{10\%}$ for the deformed Star 6 image is expressed as $l_{10\%} = 10 + 290/3999 \cdot (X - 1)$, where X is the minimum X coordinate in px of the deformed image when the 90% signal value (in this case 4.5% strain) is achieved at the image horizontal center line-cut as it is shown in Figure 10.

Comparison of the DIC and DIC-PDDO strain on the Star 6 synthetic image is pre-sented in Figure 10. The VSG size of 81 px for DIC and absolute horizon diameter of $2\delta = 140$ px for DIC-PDDO are selected to achieve the same spatial resolution at cutoff period of $l_{10\%} = 207$ px (X = 2721 px).
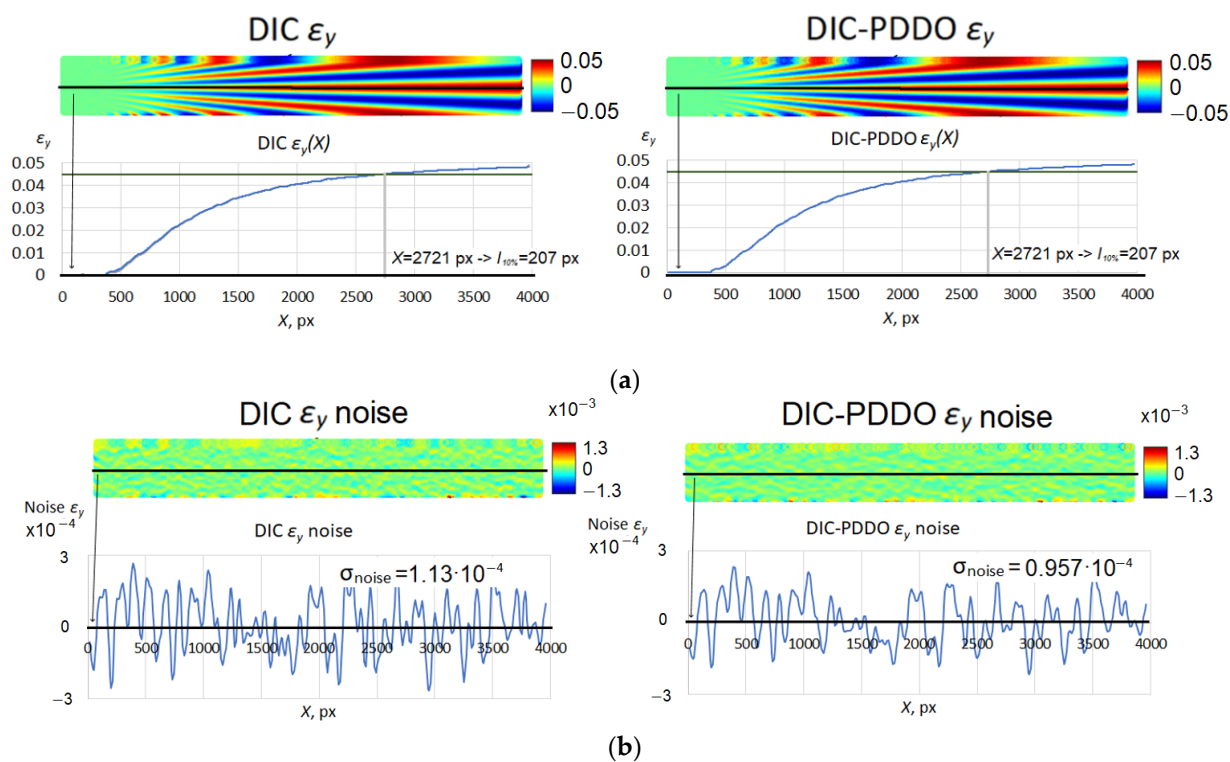

Figure 10. DIC and DIC-PDDO strain computation methods comparison using MEI: (**a**) strain fields showing the same spatial resolution of both methods for the DIC VSG = 81 px and PD $2\delta = 140$ px, (**b**) measurement resolution showing 1.2 times lower noise standard deviation in DIC-PDDO strains.

For the same spatial resolution expressed by the 10% cutoff period of 207 px, stand-ard deviations of computed strain noise levels are 1.13×10^{-4} for DIC and $0.957 \cdot 10^{-4}$ for DIC-PDDO methods resulting in 1.4 lower MEI value for the DIC-PDDO strain computa-tion method (2.65 $\mu\varepsilon^2 \cdot$px for DIC and 1.98 $\mu\varepsilon^2 \cdot$px for DIC-PDDO respectively). Figures 10 and 11 present the DIC-PDDO method comparison against conventional DIC strain cal-culation algorithms. MEI-based DIC algorithms review was graphically presented in [35] where each DIC algorithm spatial resolution (X axis) vs measurement resolution (Y axis) is plotted. Plot in Figure 11 replicates the plot from [35] by extending it with the same DIC-PDDO metrics while DIC algorithms data points from [35] are generalized and shown as grey area in the plot.
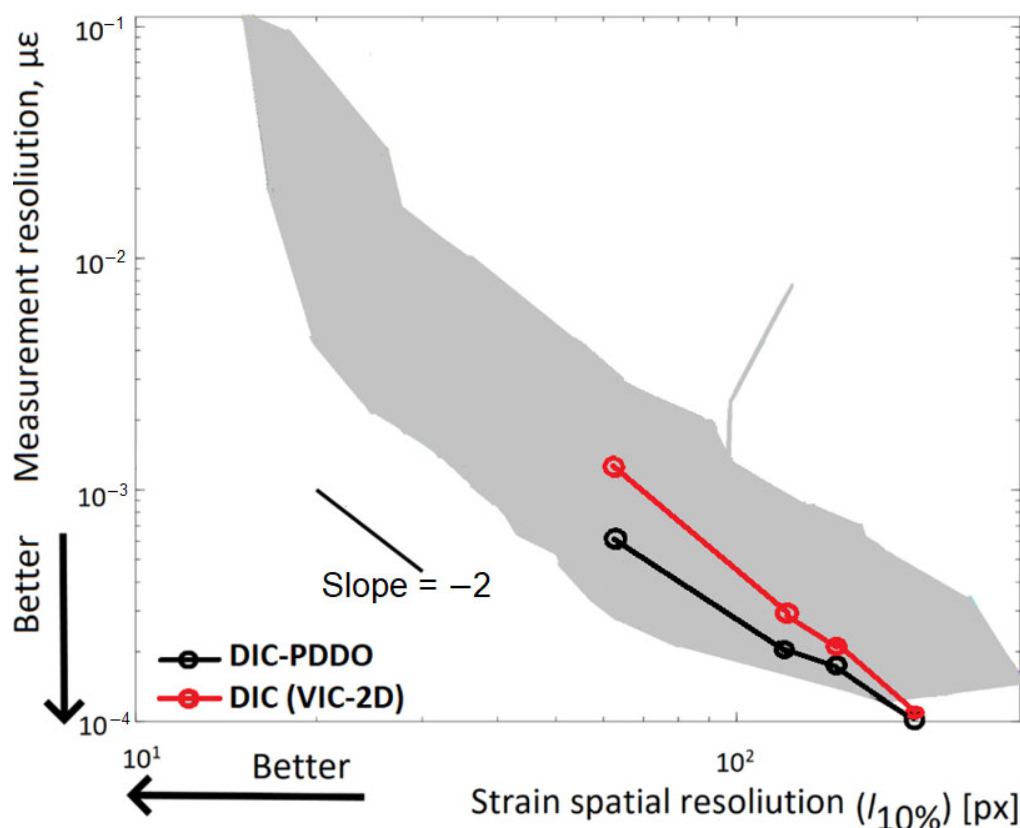
Figure 11. Comparison of the DIC strain calculation algorithms (the data points replicated from [35] are marked as grey area) and DIC-PDDO method.

The proposed PDDO strain calculation method for DIC has higher measurement resolution than the DIC VIC-2D software algorithm for each selected spatial resolution value as it is seen in Figure 11. Moreover, increasing DIC-PDDO performance with the strain spatial resolution (differences between the "DIC-PDDO" and "DIC (VIC-2D)" curves) shows the proposed method potential to accurately compute localized strains.

4.4. DIC-PDDO for Noise Reduction

In order to analyze the performance of the DIC-PDDO method for strain calculation on the tensile experiment specimen in the case of high gradients, similarly as in [12–14] (see Figure 1), the minimum DIC VSG size of 33 px (step 1 px) was used for the selected subset size. This DIC calculation setup results in an almost invisible displacement oscillations of 2 μm magnitude (0.1% of the maximum value) (the oscillations are also called as artificial noise in this study and calculated based on the comparison against the DIC displacement field generated with the DIC step of 7 px used in previous calculations (Figures 7–9) while the effect of real noise from experimental setup is not considered) (Figure 12a) which in turn results in an artificial significant noise of the DIC-calculated ε_x strains of ±0.006 units (33% of the maximum absolute value) (Figure 12b). The strain ε_x was selected for this evaluation because it is more affected by artificial noise (ε_y strains are up to 7 times higher than ε_x strains and thus the noise effect on the ε_y strains is the same times smaller). The smooth profile of the curve labeled the "PDDO to noisy DIC" in Figure 12 b shows the ability of the PDDO to eliminate the effect of the oscillatory DIC input displacements on the PDDO calculated strains as opposed to the DIC method of strain calculation which amplifies the slightly oscillatory input in the calculated strains (curve labeled "DIC noisy" in Figure 12b).
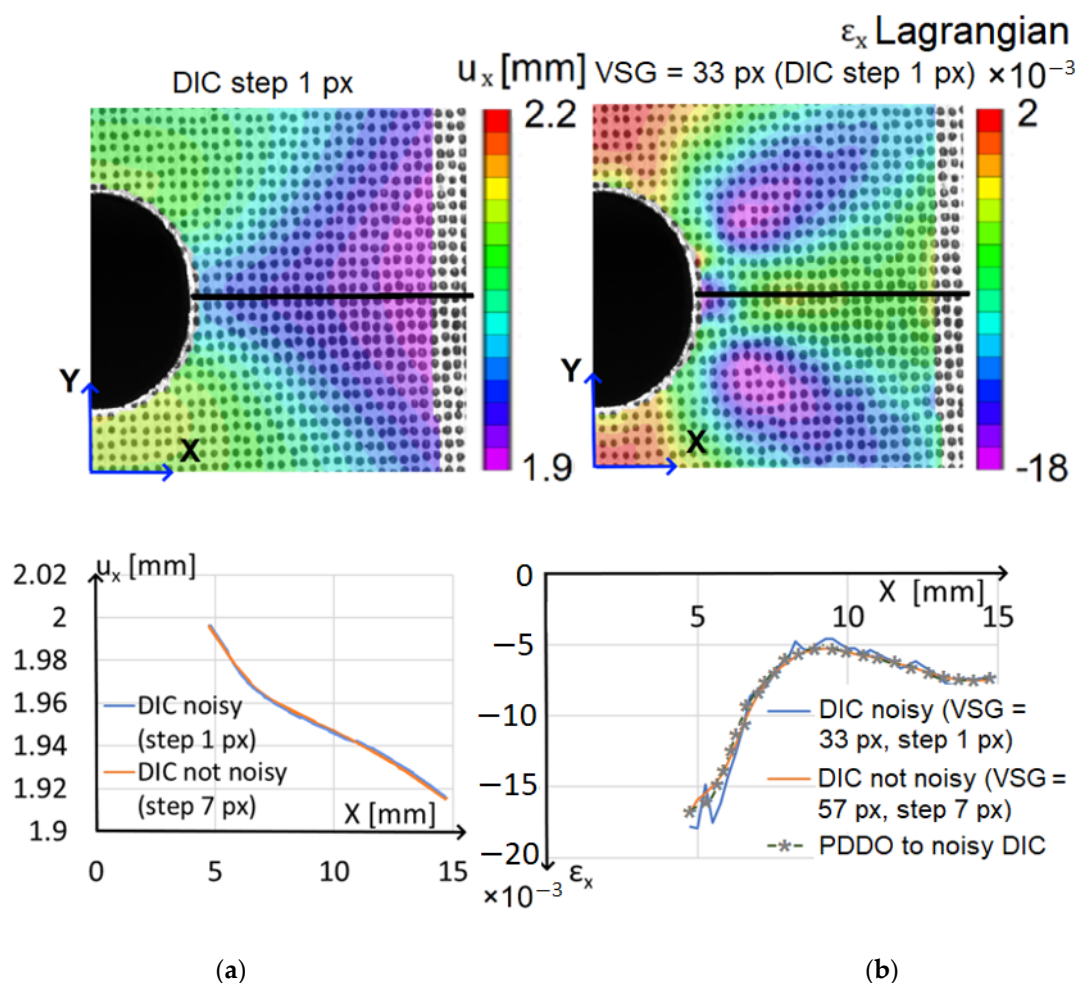
Figure 12. Slight oscillations (artificial noise) introduced in the DIC displacement (**a**), resulting in considerable noise in the DIC strains (**b**).

Similar conclusion can be done based on the observation of the PDDO application to synthetic image no. 6 of the plate with hole from DIC Challenge 1.0 Sample 12 (Figure 13, also see Figure 1). While the smaller DIC VSG leads to an oscillatory solution and larger VSG smooths out the strain peaks also reducing the strain spatial resolution, the PDDO solution provides smooth and still accurate strain profile preserving its spatial resolution.

The data in Figure 12 represent a snapshot during the specimens deformation, corresponding to 75% of the failure load (DIC image no. 60 in the set of DIC images recorded during deformation). In order to analyze the proposed PDDO method at different levels of deformation, strains were also analyzed at different loading levels of the specimen, from the test start to the specimens failure (DIC image no. 80), and results are plotted in Figure 14. The plots in Figure 14 show increasing absolute differences between the curves with the deformation due to selected artificial noise generation method and the PDDO method is able to eliminate the effects of the input noise at various deformation levels.
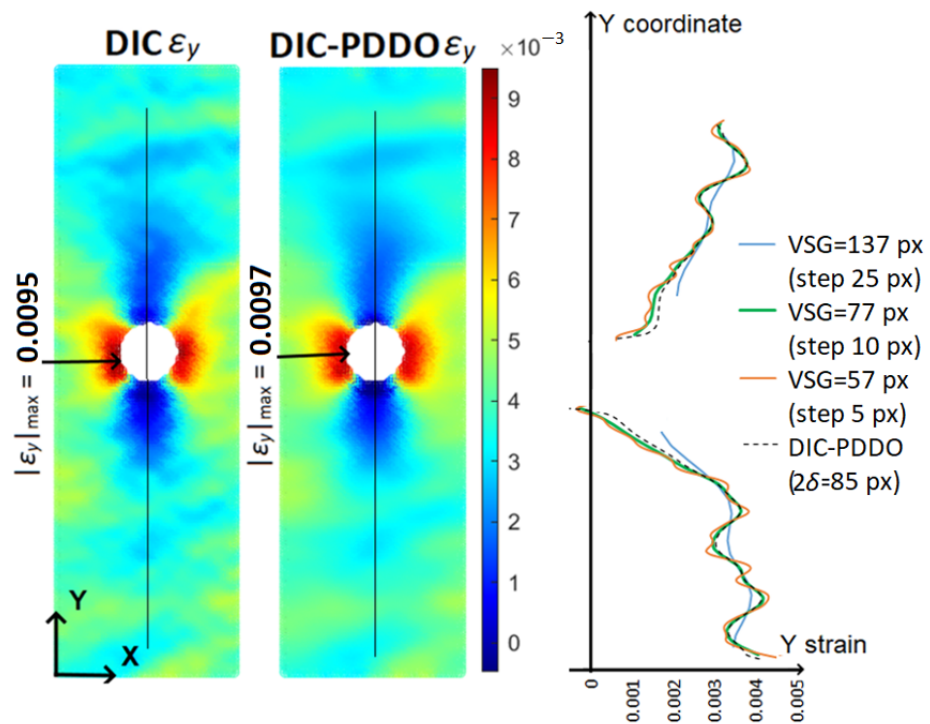
Figure 13. The problem of plate with hole analyzed in [12–14] (also see Figure 1) extended by the DIC-PDDO strain solution.
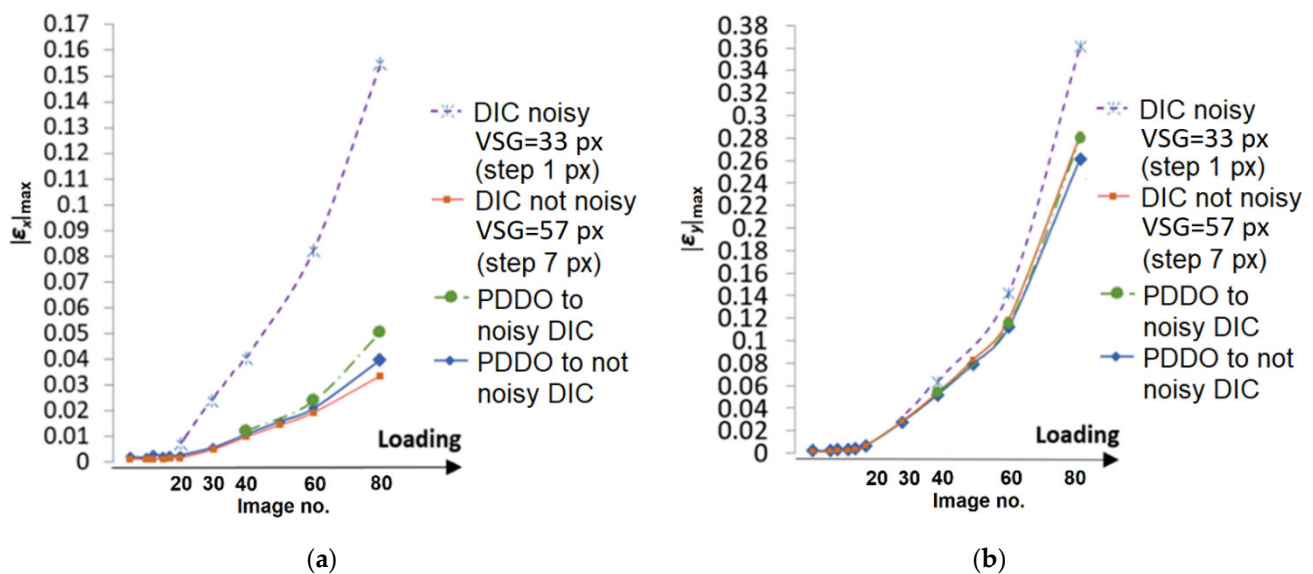

(**a**)

(**b**)

Figure 14. Effect of the input noise on the calculated strains at different levels of deformation: (**a**) ε_x strains, (**b**) ε_y strains.

The DIC method to reduce the noise in the calculated strains is the DIC strain filter (see Figure 3b) which smoothen the calculated strains by averaging over the strain filter area, and reduces thus the noise fluctuations. However, the possibility exists that the real strain peaks and strain gradients are also averaged out by using the DIC strain filter, and the DIC user should carefully select between noisy and smooth but less accurate results [41] (see Section 2.1). The results of our study show that not only the PDDO method provides a smoother (less oscillatory) strain solution (Figures 10–14), but it also preserves the accuracy of the results, as shown in Figure 15. Here the same strain field results, namely the "noisy DIC" generated by using a DIC step size of 1 px (Figure 15a), the "PDDO to

noisy DIC" generated by applying the PDDO to the slight oscillatory input displacements from the "noisy DIC" setup (Figure 15b), and the "not noisy DIC" generated by using a DIC step size of 7 px (Figure 15 c), are analyzed.
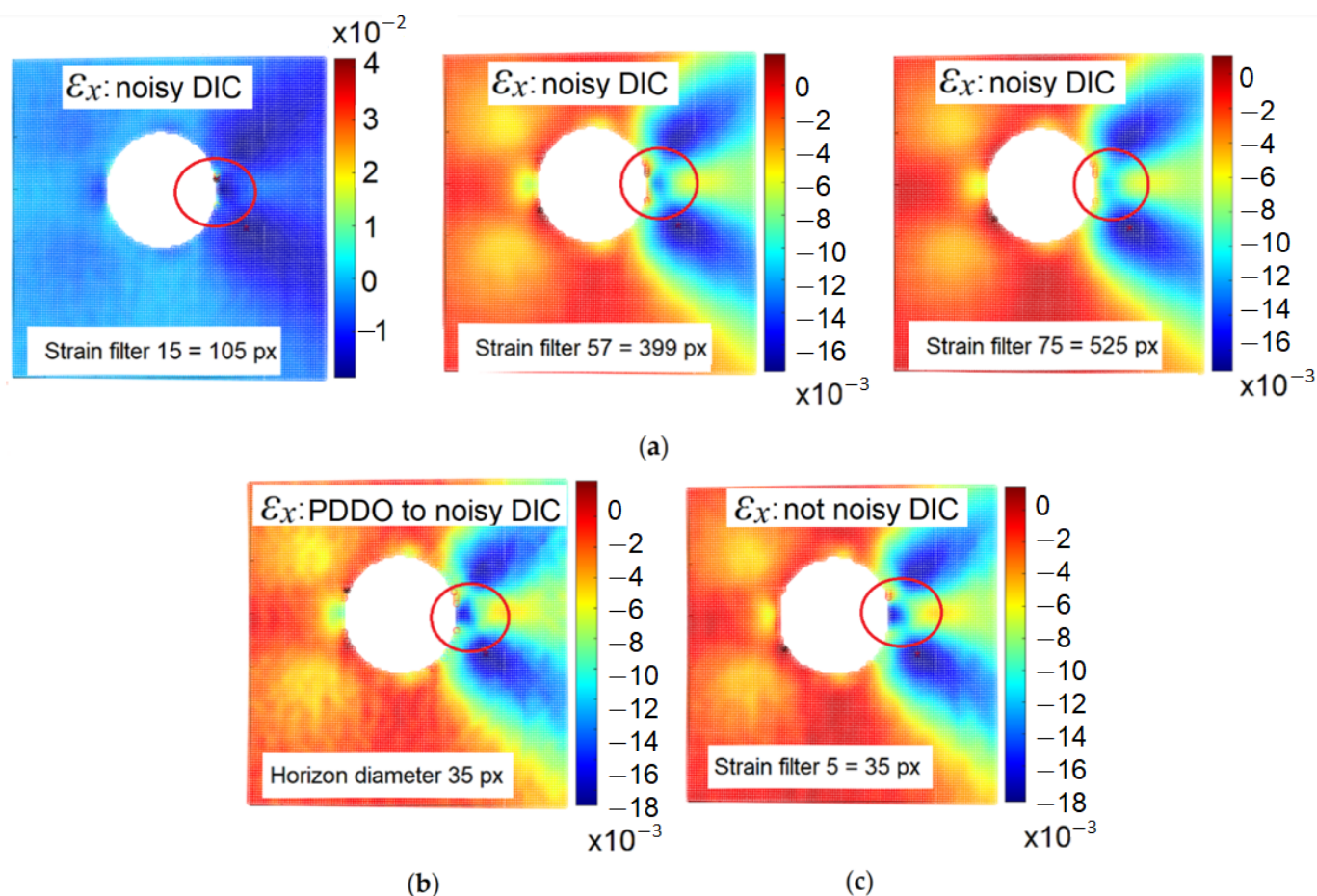

Figure 15. Strain field results: (**a**) noisy DIC; (**b**) PDDO to noisy DIC; (**c**) not noisy DIC.

The DIC strain filter of size 15 does not effectively reduce the generated noise (Figure 15 a left) resulting in almost 20 times higher maximum absolute strain value than the accurate DIC values in Figure 15c. Only by increasing the DIC strain filter size up to 57 or 75 reduces the generated noise, but the peak values of strains are lost (see red circle in Figure 15). On the contrary, the results obtained by applying the PDDO to the noisy DIC displacement data do not lose the peak values (Figure 15b). Thus, it can be concluded that the PDDO method applied to noisy DIC displacement data can filter the input noisy data and smoothen the results while not losing the strain resolution due to filtering as it is the case for the DIC strain filter. Based on this feature, the PDDO can be considered for implantation in DIC calculation software, as an alternative method to the ones currently existing in different DIC software for the DIC strain evaluation (e.g., based on displacement shape functions, strain shape functions, strain filters, etc.,).

5. Summary and Conclusions

The improvement of the DIC strain calculation algorithm based on the PDDO was analyzed in this study. Several conclusions can be underlined based on our results.

1. Although displacements can be directly and accurately measured by DIC, the strain field requires additional post processing–numerical differentiation. This mathematical operation is problematic in the case of discrete displacement field measured by the DIC in the case of high strain gradients, and also induces noise in the calculated

strains. Because of this, there is a need for better differentiation algorithms for the raw displacement data provided by the DIC. The PDDO based on the PD theory integral equations offers an alternative approach to cope with the aforementioned numerical differentiation issues. A differentiation algorithm based on the integro-differential PDDO can be formulated and applied to the DIC displacement field for strain calculation.

2. The PDDO strain calculation method was validated considering the synthetic images from DIC Challenge [11] and in-house experimental measurements. The PDDO-calculated strains and DIC-calculated strains converge to each other, and to the FE validation calculated strains, when reducing the PD grid spacing and PD horizon size for the PDDO calculation, and the DIC VSG size for the DIC calculation. Based on the PDDO evaluation using MEI, the proposed strain calculation method for DIC resulted in at least 40% lower MEI values and thus at the same time better performance than conventional DIC algorithm used in VIC-2D software. Moreover, the PDDO method efficiency is prone to be increasing for the case of localized strains (e.g., when high spatial resolution is required).

3. Analysis of both synthetic and experimental DIC images showed that the PDDO method can effectively reduce the effect of the noisy input (displacement) data on the calculated strain field, while the DIC method of strain evaluation amplifies the effect of the input data of the calculated strains. Moreover, the PDDO method has the ability to preserve the accuracy of the strain results calculated based on oscillatory/noisy input data, while the DIC strain filter smooths out the localized strain values (high strain gradients).

4. Reducing the DIC VSG size induces oscillations for the DIC-calculated strain fields and then high strain gradients cannot be effectively captured by the DIC. The aforementioned problem can be solved applying PDDO method to DIC displacement field calculated with the same small VSG size, and owing to the PDDO method DIC measurements spatial resolution can be increased without changing the DIC setup (speckle size, cameras).

References

1. Pan, B.; Qian, K.; Xie, H.; Asundi, A. Two-Dimensional Digital Image Correlation for in-Plane Displacement and Strain Measurement: A Review. *Meas. Sci. Technol.* **2009**, *20*, 062001.
2. Correlated Solutions. DIC System. Available online: https://www.correlatedsolutions.com/digital-image-correlation/ (accessed on 4 February 2022).
3. Schreier, H.; Orteu, J.-J.; Sutton, M.A. *Image Correlation for Shape, Motion and Deformation Measurements*; Springer: Boston, MA, USA, 2009.
4. Iadicola, M.; Banerjee, D. A Comparison of Strain Calculation Using Digital Image Correlation and Finite Element Software. *J. Phys. Conf. Ser.* **2016**, *734*, 032013.

5. Correlated Solutions. Digital Image Correlation Compared to Strain Gauge. Available online: http://www.correlatedsolutions.com/wp-content/uploads/2014/New Customer Docs/Vic-3D vs Strain Gauge.pdf (accessed on 15 February 2022).
6. McCluskey, M. Error Characterization for Digital Image Correlation Measurements in Industrial Environments. Master's Thesis, Aalto University, Espoo, Finland, 2017.
7. Bornert, M.; Brémand, F.; Doumalin, P.; Dupré, J.C.; Fazzini, M.; Grédiac, M.; Hild, F.; Mistou, S.; Molimard, J.; Wattrisse, B.; et al. Assessment of Digital Image Correlation Measurement Errors: Methodology and Results. *Exp. Mech.* **2009**, *49*, 353–370.
8. Siebert, T.; Becker, T.; Spiltthof, K.; Neumann, I.; Krupka, R. Error Estimations in Digital Image Correlation Technique. *Appl. Mech. Mater.* **2007**, *8*, 265–270.
9. Luo, J.; Ying, K.; He, P.; Bai, J. Properties of Savitzky–Golay Digital Differentiators. *Digit. Signal Process.* **2005**, *15*, 122–136.
10. Pan, B. Full-Field Strain Measurement Using a Two-Dimensional Savitzky-Golay Digital Differentiator in Digital Image Correlation. *Opt. Eng.* **2007**, *46*, 033601.
11. DIC Challenge. Test Images. Available online: https://idics.org/challenge/ (accessed 20 June 2022).
12. Turner, D.; Lehoucq, R.; Reu, P. A Nonlocal Strain Measure for DIC. *Conf. Proc. Soc. Exp. Mech. Ser.* **2016**, *3*, 79–83.
13. Turner, D. *Towards DIC Methods Robust Enough to Characterize Degradation of Materials*; Sandia National Lab.: Albuquerque, NM, USA, 2015.
14. Turner, D. *How Nonlocal Formulations Are Changing the Modeling and Simulalation Landscape at Sandia*; Sandia National Lab.: Albuquerque, NM, USA, 2017.
15. RReu, P.L.; Toussaint, E.; Jones, E.; Bruck, H.A.; Iadicola, M.; Balcaen, R.; Turner, D.Z.; Siebert, T.; Lava, P.; Simonsen, M. DIC Challenge: Developing Images and Guidelines for Evaluating Accuracy and Resolution of 2D Analyses. *Exp. Mech.* **2018**, *58*, 1067–1099.
16. Passieux, J.C.; Bugarin, F.; David, C.; Périé, J.N.; Robert, L. Multiscale Displacement Field Measurement Using Digital Image Correlation: Application to the Identification of Elastic Properties. *Exp. Mech.* **2015**, *55*, 121–137.
17. Zhao, J.Q.; Zeng, P.; Pan, B.; Lei, L.P.; Du, H.F.; He, W.B.; Liu, Y.; Xu, Y.J. Improved Hermite Finite Element Smoothing Method for Full-Field Strain Measurement over Arbitrary Region of Interest in Digital Image Correlation. *Opt. Lasers Eng.* **2012**, *50*, 1662–1671.
18. Zhu, Q.; He, W.; Zhu, J.; Zhou, Y.; Chen, L. Investigation on Interfacial Fracture Toughness of Plasma-Sprayed TBCs Using a Three-Point Bending Method. *Surf. Coatings Technol.* **2018**, *353*, 75–83.
19. Qian, W.; Zhang, H.; Zhu, J.; Li, J.; Zhang, J.; Zhang, M. Determination of Fracture Toughness of Polymer Coating Using Micro-Scale Digital Image Correlation Technique. *Polym. Test.* **2021**, *93*, 106896.
20. Chen, J.; Hu, X.; Ji, X. Study on Two-Step Extended Digital Image Correlation Method and Its Application. In Proceedings of the ICEM 2008: International Conference on Experimental Mechanics 2008, Nanjing, China, 8–11 November 2008; Volume 7375, pp. 1200–1204.
21. Fagerholt, E.; Børvik, T.; Hopperstad, O.S. Measuring Discontinuous Displacement Fields in Cracked Specimens Using Digital Image Correlation with Mesh Adaptation and Crack-Path Optimization. *Opt. Lasers Eng.* **2013**, *51*, 299–310.
22. Yang, J.; Bhattacharya, K. Fast Adaptive Mesh Augmented Lagrangian Digital Image Correlation. *Exp. Mech.* **2021**, *61*, 719–735.
23. Yang, J.; Bhattacharya, K. Augmented Lagrangian Digital Image Correlation. *Exp. Mech.* **2019**, *59*, 187–205.
24. Poissant, J.; Barthelat, F. A Novel "Subset Splitting" Procedure for Digital Image Correlation on Discontinuous Displacement Fields. *Exp. Mech.* **2010**, *50*, 353–364.
25. Han, J.; Pan, B. A Novel Method for Measuring Discontinuous Deformation in Digital Image Correlation Based on Partition and Dividing Strategy. *Eng. Fract. Mech.* **2018**, *204*, 185–197.
26. Silling, S. Reformulation of Elasticity Theory for Discontinuities and Long-Range Forces. *J. Mech. Phys. Solids* **2000**, *48*, 175–209.
27. Agwai, A.; Guven, I.; Madenci, E. Predicting Crack Propagation with Peridynamics: A Comparative Study. *Int. J. Fract.* **2011**, *171*, 65–78.
28. Ha, Y.; Bobaru, F. Studies of Dynamic Crack Propagation and Crack Branching with Peridynamics. *Int. J. Fract.* **2010**, *162*, 229–244.
29. Madenci, E.; Barut, A.; Futch, M. Peridynamic Differential Operator and Its Applications. *Comput. Methods Appl. Mech. Eng.* **2016**, *304*, 408–451.
30. Madenci, E.; Barut, A.; Dorduncu, M. *Peridynamic Differential Operator for Numerical Analysis*; Springer International Publishing: Cham, Switzerland, 2019.
31. Madenci, E.; Barut, A.; Willmarth, E.; Phan, N. Peridynamics for Data Estimation, Image Compression/Recovery, and Model Reduction. *J. Peridyn. Nonlocal Model.* **2022**, *4*, 159–200.
32. Madenci, E.; Yaghoobi, A.; Barut, A.; Phan, N.; Iliopoulos, A.; Michopoulos, J.G. Peridynamics Enabled Digital Image Correlation for Tracking Crack Paths. *Eng. Comput.* **2022**. https://doi.org/10.1007/s00366-021-01592-4.
33. Turner, D. Peridynamics-Based Digital Image Correlation Algorithm Suitable for Cracks and Other Discontinuities. *J. Eng. Mech.* **2015**, *141*, 04014115.
34. Li, T.; Gu, X.; Zhang, Q.; Lei, D. Coupled Digital Image Correlation and Peridynamics for Full-Field Deformation Measurement and Local Damage Prediction. *Comput. Model. Eng. Sci.* **2019**, *121*, 425–444.

35. Reu, P.L.; Blaysat, B.; Andó, E.; Bhattacharya, K.; Couture, C.; Couty, V.; Deb, D.; Fayad, S.S.; Iadicola, M.A.; Jaminion, S.; et al. DIC Challenge 2.0: Developing Images and Guidelines for Evaluating Accuracy and Resolution of 2D Analyses. *Exp. Mech.* **2022**, *62*, 639–654.

36. Blaysat, B.; Neggers, J.; Grédiac, M.; Sur, F. Towards Criteria Characterizing the Metrological Performance of Full-Field Measurement Techniques: Application to the Comparison Between Local and Global Versions of DIC. *Exp. Mech.* **2020**, *60*, 393–407.

37. Digitalimagecorrelation.org. A Practical Guide to DIC. Available online: https://digitalimagecorrelation.org/#patterning (accessed on 5 Feburary 2022).

38. International Digital Image Correlation Society, Jones, E.M.C. and Iadicola, M.A. (Eds.). A Good Practices Guide for Digital Image Correlation. Available online: http://idics.org/guide/ (accessed on 18 February 2022).

39. Correlated Solutions. Minimizing Noise and Bias in 3D DIC. Available online: http://www.correlatedsolutions.com/supportcontent/dic-noise-bias.pdf (accessed on 28 February 2022).

40. Correlated Solutions. VIC-3D Reference Manual. Available online: http://www.correlatedsolutions.com/supportcontent/VIC-3D-8-Manual.pdf (accessed on 23 February 2022).

41. Correlated Solutions Knowledgebase. Application Note AN-1703 Strain Filter Selection. 2018, *Accept*.

42. Correlated Solutions. Subset, Step Size and Strain Filter Selection. Available online: https://correlated.kayako.com/article/44-subset-step-size-and-strain-filter-selection (accessed on 19 February 2022).

43. Madenci, E.; Yaghoobi, A.; Barut, A.; Phan, N. Peridynamics/Digital Imaging Correlation for Tracking Crack Propagation Paths. Presented at the IMECE 2018, Pittsburgh, PA, USA, 9–15 November 2018.

44. Wang, B.; Oterkus, S.; Oterkus, E. Determination of Horizon Size in State-Based Peridynamics. *Contin. Mech. Thermodyn.* **2020**. https://doi.org/10.1007/s00161-020-00896-y.

45. Silling, S.; Epton, M.; Weckner, O.; Xu, J.; Askari, E. Peridynamic States and Constitutive Modeling. *J. Elast.* **2007**, *88*, 151–184.

46. DIBOND. DIBOND Composite. Available online: https://www.barefootkitchens.com.au/composite/5495-dibond-brochure.html (accessed on 8 January 2022).

47. MATLAB Peridynamics open Source Code. Available online: https://github.com/chtld/BB_PD (accessed on 4 January 2022).

48. Livermore Software Technology Corporation (LSTC). LS-DYNA Keyword User' S Manual. Available online: https://www.dynasupport.com/manuals (accessed on 21 Feburary 2022).